PHYSICAL REVIEW B VOLUME 16, NUMBER 8 15 OCTOBER 1977

Raman and infrared studies of superlattice formation in $TiSe_2$†

J. A. Holy,* K. C. Woo, M. V. Klein, and F. C. Brown
Department of Physics and Materials Research Laboratory, University of Illinois at Urbana-Champaign, Urbana, Illinois 61801
(Received 9 June 1977)

Raman and far-infrared reflectivity spectra have been obtained for both stoichiometric and nonstoichiometric $TiSe_2$ above and below the transition temperatures corresponding to formation of the $2a_0 \times 2c_0$ superlattice. In the normal phase above T_c Raman-active lines are observed at 134 cm^{-1} (E_g) and at 195 cm^{-1} (A_{1g}). Normal-incidence reflectivity shows a single E_u mode at 137 cm^{-1} superimposed upon a highly damped Drude background. Below T_c, strong new E_g and A_{1g} Raman lines appear together with several weaker lines and bands. Likewise, a Kramers-Kronig analysis of the low-temperature infrared data shows many new optically active lattice modes. We have predicted the number and symmetry of all even and odd modes which are folded into the center of the original Brillouin zone from the points A, L, and M at the zone surface due to the periodic lattice distortion. Reasonable agreement is found for the suggested superlattice, although some weak lines in both the low-temperature Raman and infrared data are unexplained.

I. INTRODUCTION

The group-IVb dichalcogenides crystallize in a $1T$ hexagonal layer structure in which the transition metal is octahedrally coordinated. A wide range of physical properties exists through the group, for example TiS_2 and $TiSe_2$ tend to be degenerate semiconductors or semimetals, whereas the zirconium and hafnium compounds are insulators. Recent careful band calculations on $TiSe_2$,[1] as well as experimental work, indicate nearly overlapping valence maxima and conduction-band minima (at Γ and L respectively).

Bonding in the titanium compounds is largely covalent with appropriate admixture of s, p, and d wave functions. In some respects the situation is like the molecular-orbital results described by Wilson and Yoffe,[2] except there is little or no gap between s-p valence bands and d-like conduction bands. The conduction and valence bands of $TiSe_2$ actually overlap slightly so that the stoichiometric compound is a semimetal with about 10^{20} carriers/cm^3.[3] The overlap has been directly observed by means of angle-resolved photoemission[4] in $TiSe_2$ crystals containing excess Ti and such work is underway on stoichiometric material.[5]

$TiSe_2$ is especially interesting in that a number of groups have observed a $2a_0 \times 2c_0$ superlattice which sets in below $T_c = 200$ °K in stoichiometric material[3,6] and around 150 °K in crystals containing 1.5–2% excess Ti.[7–9] Strong fluctuations in the $2a_0$ lattice are observed by x-ray or electron diffraction well above T_c. The phase transition is of second order and appears to involve charge-density waves whose wave vector $\vec{q}$ links the center of the zone Γ with points L out of the midplane on the zone edge.[3] Wilson and Mahajan have suggested[6] that coupling of electrons at L and holes at Γ is important and that $TiSe_2$ is a "pathway to the excitonic state of matter". Whether this is true or not, the resistivity measurements[10] on TiS_2 probably can be understood in terms of strong electron-hole scattering.[11]

Superlattice formation should have a dramatic effect on the vibrational spectrum of a crystal and on the number of Raman and infrared-active modes observed. In fact, Liang *et al.*[8] show room-temperature reflectivity spectra for $1T$-$TaSe_2$ which has a commensurate charge-density wave. A number of sharp features are seen in the spectrum at long wavelengths (~200 cm^{-1}). Woo and coworkers[7] give similar reflectivity spectra for nonstoichiometric $TiSe_2$ above and below T_c, and striking changes are observed due to superlattice formation. In this paper, we present Raman and infrared reflectivity data on both stoichiometric and nonstoichiometric $TiSe_2$ crystals. The Raman data extend from room temperature, which is above T_c, down to 53 °K, well below T_c. Far-infrared reflection was studied down to about 20 °K. Thus evolution of the spectra can be followed through the transition temperature.

Figure 1 shows the normal-crystal structure of $1T$-$TiSe_2$. Notice the layer structure consisting of Se-Ti-Se sandwiches and octahedral coordination of Ti. There is one formula unit (3 atoms) per unit cell—each figure shows two unit cells. The structure has the nonsymmorphic space group D_{3d}^3 with the Ti atoms at centers of inversion. There are nine zone-center vibrational modes for $1T$-$TiSe_2$ with three atoms per unit cell.[12] Decomposition of the displacements of the three atoms into irreducible representations yields the following result for the Γ point:

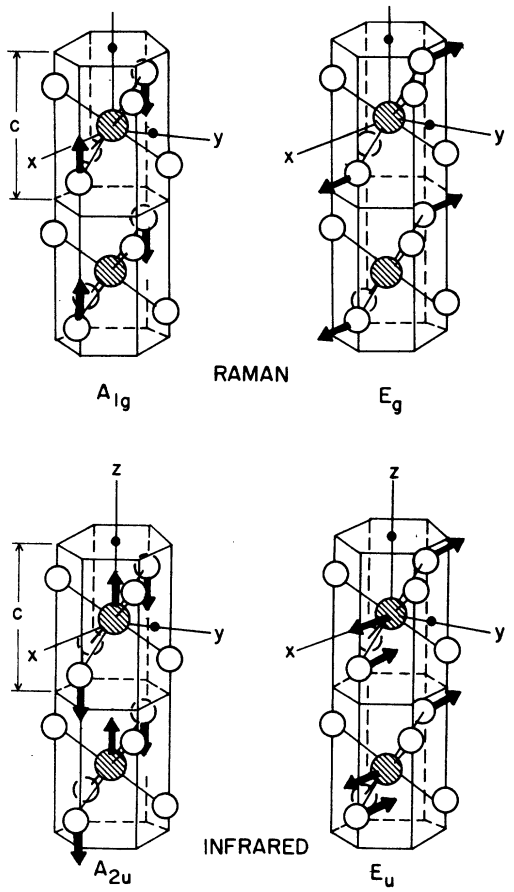

FIG. 1. Crystal structure of 1T layered compounds. Raman-active modes are shown in the upper part of the Figure; infrared-active modes in the lower.

$$\Gamma = A_{1g} + E_g(2) + 2A_{2u} + 2E_u(2) \,. \tag{1}$$

There are two Raman-active $k=0$ phonon modes expected for this lattice; an A_{1g} mode in which the two Se atoms per unit cell move relative to one another along the z axis, and a doubly-degenerate E_g mode in which the Se atoms move opposite to one another along x or along y directions. The displacements for these two types of Raman-active modes are shown in the upper part of Fig. 1.

The four odd-parity modes of Eq. (1) are divided into two acoustic and two optic modes. The acoustic modes in the vicinity of $k=0$ have been studied by Stirling *et al.*[13] using inelastic neutron diffraction.

Displacements for the infrared-active A_{2u} and (x,y)-degenerate E_u modes are shown in the lower part of Fig. 1. The A_{2u} mode is polarized along the z axis and consequently requires an electric vector $\vec{E}$ parallel to the c axis or oblique incidence. Only the single E_u mode should be seen in reflection for light propagating normal to the layer plane, and the resulting peak in the imaginary part of the dielectric constant should occur at the familiar transverse optical frequency. Results are given in Sec. III, and we will see that this TO frequency occurs at about 137 cm^{-1}.

The unit cell for the $2a_0 \times 2c_0$ superlattice[3] contains 24 rather than three atoms, therefore we expect 8 times as many $k=0$ phonon modes in the distorted structure. Displacement patterns having the correct symmetry may be generated for the new modes from the eigenvectors of those zone-boundary phonons whose wave vectors fold to $k=0$. This is discussed in Sec. IV using a method which is analogous to the correlation method of molecular spectroscopy. It leads to a complete enumeration of the new modes and their symmetries and to a correlation between properties of the new modes and of the zone-boundary phonons that generate them. Results given in Sec. III are analyzed in Sec. V. We turn to a brief discussion of the experimental methods in the next section.

II. EXPERIMENTAL METHODS

Several batches of $TiSe_2$ were grown in evacuated quartz tubes by the standard vapor transport techniques.[14] Stoichiometry is critically dependent upon growth temperature, and nonstoichiometric crystals are characterized by charge-density-wave transition temperatures less than 200 K. The present work was carried out on two batches of crystals; the first grown below 550 °C had a transition temperature $T_c \sim 200$ K; the second was grown at 800 °C and had $T_c \sim 150$ K, corresponding to 1.5–2% excess Ti. X-ray diffraction showed the 1T-CdI_2 structure. Samples were cleaved just before inserting in cryostats for Raman or infrared reflectivity measurements.

The Raman spectra were excited by a 200–300-mW beam at 5145 Å from an argon-ion laser. The laser beam was incident onto the layer (0001) plane at the psuedo-Brewster's angle. Scattered light was collected along the c axis and analyzed using a double grating monochromator equipped with a third monochromator. Low temperature runs were made with a "Helitran" cryostat modified to hold the sample in an inner chamber having cold windows. The sample was cooled by flowing helium gas, and nominal temperatures were measured with a thermocouple. Temperatures with the laser beam were substantially higher than at the thermocouples; they were determined from the ratio of anti-Stokes to Stokes Raman intensities.

A Beckman IR-11 spectrophotometer was used to measure the far infrared reflectivity from 120 to 350 cm^{-1}. A Fourier interferometer with a doped-germanium bolometer operating at 1.5 K and

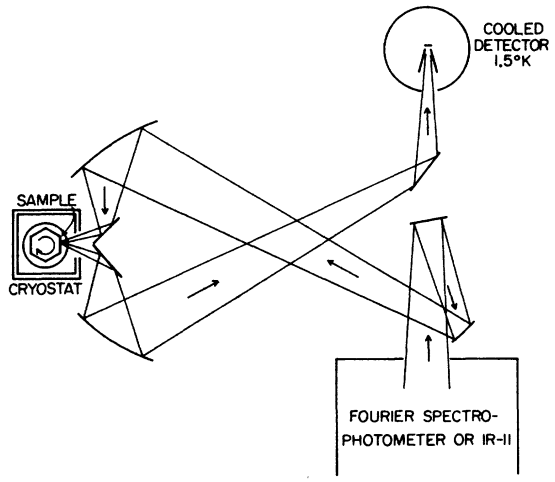

FIG. 2. Arrangement of source, beam condensing mirrors, sample, and detector for far-infrared reflectivity measurements.

Fourier transform techniques were used in the range 40 to 200 cm^{-1}. In both cases, small samples were accomodated in a beam condensing reflectometer which used nonspherical optics as described by Brandt.[15] As shown in Fig. 2, the sample and an aluminum mirror could be rotated into the beam for measurements at near normal incidence without altering the path through polyethylene windows of the cryostat. Dry nitrogen gas was used for flushing the light path outside these windows. The polarization was confirmed to be that for E_u modes by use of a wire-grating polarizer. Sample temperature was determined by copper *versus* constantan and gold-iron *versus* chromel thermocouples.

In most cases, the infrared reflection of the sample was first recorded at room temperature and then either at liquid nitrogen (88 K) or at liquid-helium sample temperature (20 K) without otherwise disturbing the experimental set-up. Finally, the aluminum mirror was rotated into the beam and its reflection spectrum recorded. In sorting out structure, it was helpful to take the ratio of the low-temperature sample reflectivity to that at room temperature. Likewise the reflectivity of the sample was referred to the measured reflectivity of aluminum. The resulting structure was identical with both reference techniques and absolute reflectivity reproduced to a few percent. The data shown and all features discussed in the next section were reproduced in three or more scans. The two different spectrophotometers agreed in the overlapping range.

A Kramers-Kronig analysis of reflectivity was carried out in order to obtain the imaginary part ϵ_2 of the dielectric response function. Extrapolation to high frequencies was made using reflectivity data reported earlier[7,8] and the results of Greenaway and Nitsche.[16] At very low frequencies of less than 40 cm^{-1} the data reasonably extrapolate according to the Hagen-Rubens relation

$$R \simeq 1 - (2\omega/\pi\sigma_0)^{1/2}, \tag{2}$$

where ω is the angular frequency and σ_0 the direct current conductivity.

III. RESULTS

The results at room temperature well above T_c will be given first. Recall that one expects an E_g and an A_{1g} Raman line and at normal incidence a single E_u infrared active mode. Raman data taken at room temperature are shown in Fig. 3 with both $(x'x)$ and $(x'y)$ polarization. One clearly sees the E_g line at 134 and the A_{1g} line at 194 cm^{-1}. Here, x' and x refer to polarization directions in the plane of incidence for the incident and scattered light, respectively, and y refers to a scattered polarization direction normal to the plane of

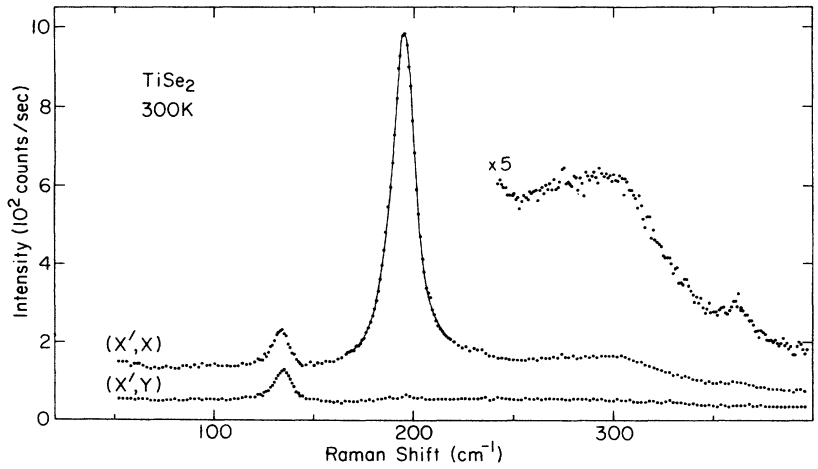

FIG. 3. Polarized Raman spectra of $1T$-$TiSe_2$ at room temperature. Laser power, 340 mW; resolution, 4 cm^{-1}; data-point interval, 1 cm^{-1}; dwell time, 20 sec.

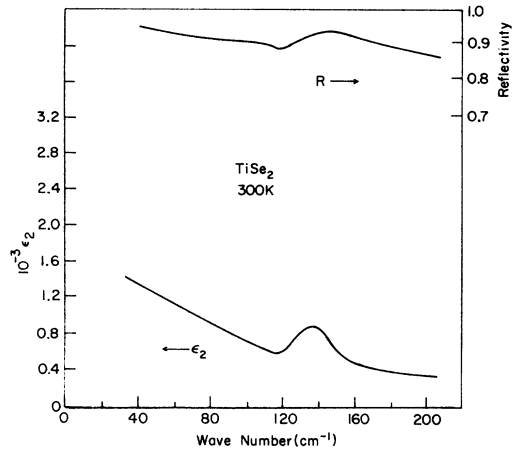

FIG. 4. Observed reflectivity and computed ϵ_2 for $TiSe_2$ at 300 K. Spectral band width 4 cm^{-1}.

TABLE I. Energies and symmetries of one-phonon and two-phonon peaks in stoichiometric 1T-$TiSe_2$ at 53 K. Single asterisk indicates modes in original lattice. Double asterisk indicates intense charge-density-wave-coupled modes. Modes with energies of 300 cm^{-1} and above are due to two-phonon processes.

ω (cm^{-1})	Symmetry	ω (cm^{-1})	Symmetry
74	E_g^{**}	187	A_{1g}
93	E_g	204	A_{1g}^{*}
114	E_g	300	A_{1g}
116	A_g^{**}	314	E_g
136	E_g^{*}	345	A_{1g}
148	E_g	377	A_{1g}
173	A_{1g}	407	A_{1g}

incidence. There are also weak A_{1g} peaks at 300 and at 360 cm^{-1} which we assign to two phonon processes. These data are similar to those of Smith *et al.*[17] Identical room temperature spectra were obtained for stoichiometric and nonstoichiometric crystals.

Figure 4 shows the observed normal-incidence reflectivity at room temperature along with the calculated ϵ_2. Notice that a single rather broad line appears at 137 cm^{-1}, the transverse optical or E_u mode. This is as previously reported for room temperature[7,8] and is little different for stoichiometric as compared to nonstoichiometric crystals.

Raman spectra were recorded for the nearly stoichiometric crystals ($T_c = 200$ K) as well as for a batch containing excess T_i ($T_c \sim 150$ K). Figure 5 shows the Raman spectrum of a stoichiometric sample with a $2a_0 \times 2c_0$ superlattice at 53 K, much below the transition temperature. There are two strong new peaks at 74 and 114 cm^{-1} in the low-frequency region and weak new peaks throughout the spectral region. The original E_g and A_{1g} modes, at 136 and 204 cm^{-1} preserve their identity. Table I lists all the Raman-active modes observed.

Figure 6 shows the temperature dependence of the new modes below 200 cm^{-1}. None of the peaks show much softening; the frequency of the strongest new E_g mode changes the most, but this change is only from 74 to 64 cm^{-1} between 53 and 147 K. This peak is much broader than other peaks and cannot be seen above 150 K. However, it probably still exists at 175 K because of the large integrated intensity remaining in the 30–100 cm^{-1} region.

The temperature dependence of the 314-cm^{-1} E_g peak in Fig. 5 is comparable to that of the strong new A_{1g} mode. Its frequency, 50% higher than the original A_{1g} mode, seems too high to result from the folding of optic phonons from boundaries of

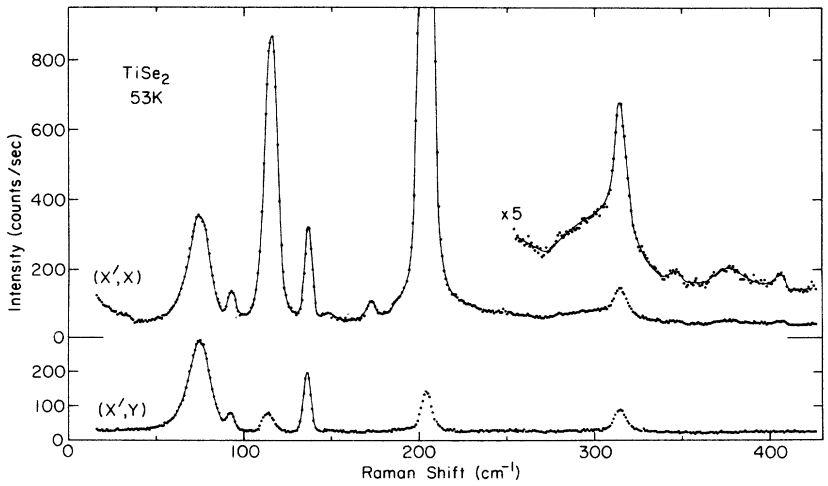

FIG. 5. Polarized spectra of stoichiometric ($T_c \approx 200$ K) 1T-$TiSe_2$ at 53 K. Laser power, 200 mW; resolution, 4 cm^{-1}; datapoint interval, 1 cm^{-1}; dwell time, 30 sec.

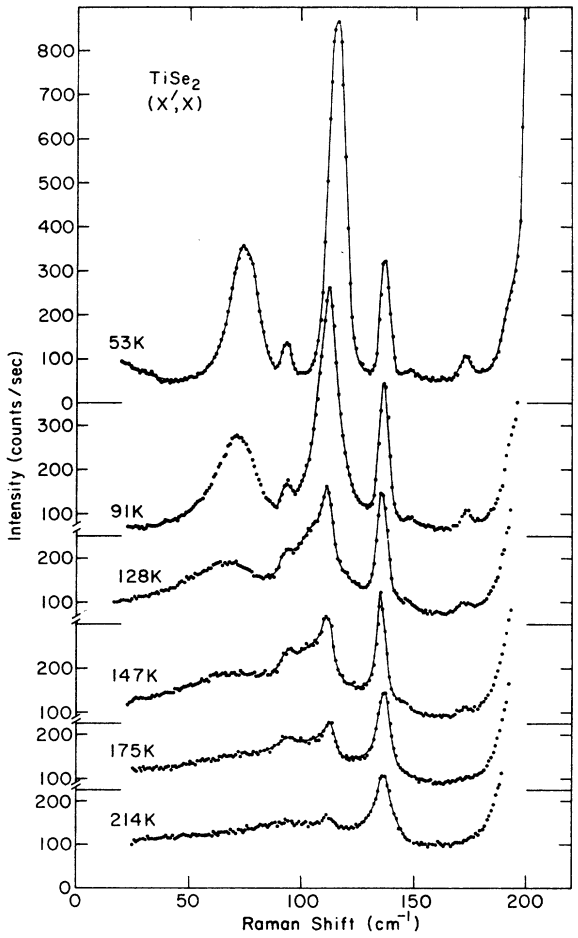

FIG. 6. Temperature dependence of the (x', x) spectrum of stoichiometric ($T_c \approx 200$ K) $1T - TiSe_2$. Laser power, 300 mW; resolution, 4 cm^{-1}; data-point interval, 1 cm^{-1}; dwell time, 20 sec, except for the 53-K curve. was recorded with 200 mW at a dwell time of 30 sec and normalized to the other curves.

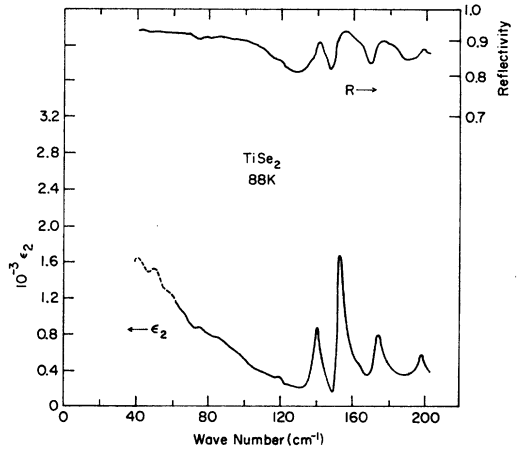

FIG. 7. Normal incidence reflectivity and computed ϵ_2 for stoichiometric $TiSe_2$ at 88 K. Spectral bandwidth, 4 cm^{-1}; the structure below 60 cm^{-1} is less reproducible and is therefore shown by a dotted line.

the Brillouin zone. It occurs in the same region as two-phonon peaks and is probably due to a two-phonon process. The original two-phonon peaks near 300 and 375 cm^{-1} are observed at 53 K, and new two-phonon peaks appear at 345 and 407 cm^{-1}.

The infrared reflectivity and computed ϵ_2 for stoichiometric $TiSe_2$ are shown in Figs. 7 and 8 for 88 and 20 K, respectively. Data were actually taken up to 350 cm^{-1} but no sharp structure was observed above 200 cm^{-1}. At 88 K it can be seen that besides the original 137 cm^{-1} band (which is now very much narrower), two strong peaks occur at about 155 and 175 cm^{-1}; a line at about 199 cm^{-1} and a weak feature at 118 cm^{-1} are also evident. At least one additional unresolved line appears at 161 cm^{-1} as a shoulder of the strong peak at 155 cm^{-1}. Moreover, weak bands can just be resolved at 45, 55, and 76 cm^{-1}. The 45- and 55-cm^{-1} bands are especially weak and barely reproducible.

At the lower temperature of 20 K, Fig. 8 shows additional infrared modes at extremely low frequency. The weak 76 cm^{-1} band is now a prominent peak between new lines at 64 and 90 cm^{-1}. It should be pointed out that the features below 65 cm^{-1} lie in a region where the interferometer beam splitter is less efficient. Apparently the 76, 90, and 118 cm^{-1} infrared modes are closely related to E_g modes at 75, 93, and 114 cm^{-1} observed in the Raman scattering at 53 K. At the lowest temperatures it appears that the 74-cm^{-1} Raman and 76-cm^{-1} infrared modes have about the same widths. This is no longer true at higher temperatures, as can be seen by comparing the 91-K curve of Fig. 6 with Fig. 7. The infrared lines at 137, 152, and 175 cm^{-1} have become noticeably higher and nar-

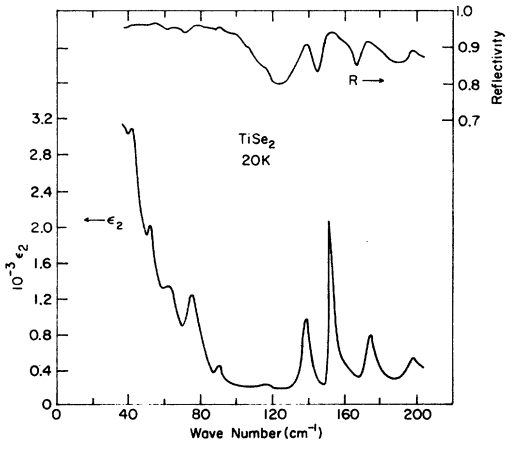

FIG. 8. Normal incidence reflectivity and ϵ_2 for a stoichiometric $TiSe_2$ crystal at 20 K. Spectral bandwidth 4 cm^{-1}.

TABLE II. The frequency of peaks observed in the ϵ_2 curve for nearly stoichiometric $TiSe_2$ at 20 K obtained from normal incidence reflectivity data. *w* indicates weak lines. The double asterisk identifies a mode which is strongly coupled to the charge-density wave as judged by its temperature dependence.

ω (cm^{-1})	Comments	ω (cm^{-1})	Comments
42	*w*	137	Original
52	*w*	152	Strong
64	*w*	162	*w*
76	**	175	
90	*w*	178	?
118	*w*	198	

rower upon cooling from 88 to 20 K. The strong lines at 152 and 175 cm^{-1} are asymmetric, and there may be additional components on their high-frequency sides. These features have been assigned the frequencies 162 and 178 cm^{-1}. All of the low temperature infrared lines are listed in Table II.

Let us now consider crystals with excess Ti. The temperature dependence of Raman scattering in the low frequency region is shown in Fig. 9 for a nonstoichiometric sample. Scans were also taken at higher frequency and the temperature dependence of the 314 cm^{-1} two phonon peak is similar to that in the stoichiometric sample when T is scaled to T_c. On the other hand, the spectrum in the low-frequency region is somewhat different. The strong new modes at 84 K in Fig. 9 at about 102 and 110 cm^{-1} have A_{1g} symmetry. Weak E_g modes were also found at 93 and 112 cm^{-1}, which are probably the 93 and 114 cm^{-1} E_g modes of the

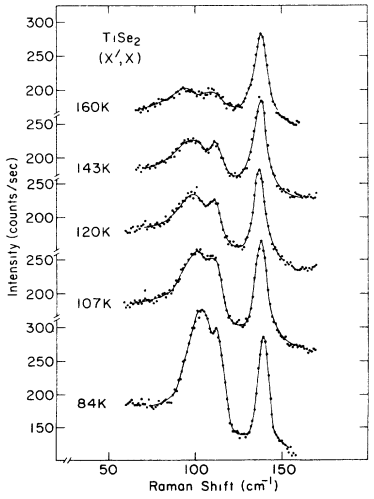

FIG. 9. Temperature dependence of the (x', x) spectrum of nonstoichiometric ($T_c \approx 150$ K) 1T-$TiSe_2$. Laser power, 300 mW; resolution, 6 cm^{-1}; data-point interval, 1 cm^{-1}; dwell time, 20 sec.

stoichiometric sample listed in Table I. The mode at 110 cm^{-1} is the strong A_{1g} mode observed below T_c in the stoichiometric sample; its intensity relative to the original E_g mode is comparable to that in the A_{1g} mode of the stoichiometric sample at the same reduced temperature. The broad A_{1g} mode at 102 cm^{-1} does not seem to have a counterpart in the low-temperature spectra of the stoichiometric sample; it shows a little softening, occuring at 84 cm^{-1} at 160 K and at 102 cm^{-1} at 84 K. The E_g mode at 74 cm^{-1} in Fig. 5 was not evident in the data down to 84 K for a nonstoichiometric sample. However, an infrared peak close to this frequency was observed in nonstoichiometric crystals at 20 K.

Infrared data at 20 K on nonstoichiometric crystals ($T_c = 150$ K) basically coincided with the results of stoichiometric crystals ($T_c = 200$ K), except in the region 90–130 cm^{-1}. The 90-cm^{-1} and weak-118-cm^{-1} peaks were not observed; instead a broad band was seen centered at about 100 cm^{-1}. These results on E_u modes for nonstoichiometric crystals are rather like the Raman results. Differences in both spectra around 100 cm^{-1} and below T_c are probably associated with excess Ti between layers.

IV. SYMMETRY ARGUMENTS APPLIED TO THE LOW-TEMPERATURE PHASE

The second-order phase transition, which occurs in stoichiometric $TiSe_2$ at about 200 K, results in a $2a_0 \times 2c_0$ superlattice, as shown by electron and x-ray diffraction[7] and by neutron diffraction[3] techniques. The transition is normal-to-commensurate charge-density-wave (CDW), and an incommensurate CDW state does not appear. The wave vectors $\vec{q}_j$ of the three simultaneously present CDW's are at the $\frac{1}{2}0\frac{1}{2}$ or L points in the Brillouin zone and are shown in Fig. 10.

Each CDW causes a displacement of L_2 symmetry of a Ti or Se atom in the basal plane per-

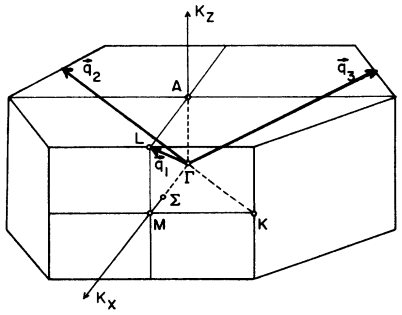

FIG. 10. Wave vectors of the three CDW's in 1T-$TiSe_2$. The x and z axes of reciprocal space are labeled by K_x and K_z, respectively.

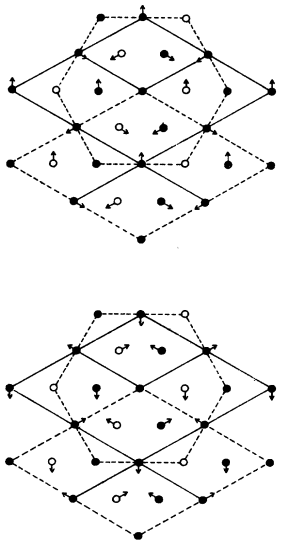

FIG. 11. Displacements of atoms in the commensurate superlattice of $1T$-$TiSe_2$ according to DiSalvo, Moncton, and Waszczak, Ref. 3. Solid circles are Ti atoms. Open circles are Se atoms above a Ti layer, and shaded circles are Se atoms below a Ti layer. Dashed lines outline conventional and Wigner-Seitz primitive cells.

pendicular to $\vec{q}_j$. We can write for the displacement of the μth atom in the ith unit cell

$$\vec{u}_\mu(\vec{R}_i) = \mathrm{Im} \sum_{j=1}^{3} \hat{q}_j^T \phi_{\mu j}^T e^{i\vec{q}_j \cdot \vec{R}_i}, \tag{3}$$

where $\hat{q}_j^T$ is a unit vector perpendicular to $\vec{q}_j$ in the basal plane and $\phi_{\mu j}^T$ are the complex amplitudes of distortion. For the Ti atom 1 and Se atoms 2 or 3 in an original unit cell, DiSalvo *et al.*[3] determined

$$\begin{aligned} |\phi_{1j}^T| &= (0.012 \pm 0.002) a_0 , \\ |\phi_{2,3j}^T| &= (0.004 \pm 0.001) a_0 , \end{aligned} \tag{4}$$

where $a_0 = 3.535$ Å is the original hexagonal lattice constant. The periodic lattice distortion involves displacements of both Ti and Se atoms in the basal plane but the metal atoms have the largest displacement. The atomic displacements forming the superlattice are shown in Fig. 11. For this structure the space group is nonsymmorphic and is D_{3d}^4. The center of inversion is at a point midway between the layers along a line through the Ti atoms at the Wigner-Seitz cell center; the horizontal reflection plane for the $2S_6$ operations is midway between layers, and $3\sigma_d$ are glide planes.

TABLE III. Normal modes of the superlattice in $1T$-$TiSe_2$.

D_{3d}	E	$2C_3$	$3C_2'$	i	$2S_6$	$3\sigma_d$
T_{72}	72	0	−4	0	0	0

$T_{72} = 5A_{1g} + 7A_{2g} + 12E_g + 5A_{1u} + 7A_{2u} + 12E_u$

The three translation vectors at each atom of the 24-atom unit cell of the superlattice generate a 72-dimensional representation. The characters of this representation and its reduction are given in Table III. There should be $5A_{1g} + 12E_g$ Raman-active modes in the superlattice, or $4A_{1g} + 11E_g$ new Raman-active modes. We actually observe four new A_{1g} modes but only five new E_g modes from one-phonon Raman processes. Table III also indicates that there should be a total of $7A_{2u} + 12E_u$ infrared active modes in the superlattice; however, only E_u modes should be observed in normal incidence reflectivity. One of the $12E_u$ modes is acoustic, and one is the optic mode of the original lattice; thus 10 new modes or a total of $11E_u$ modes should be observed. (Table II lists 12 frequencies, although at least one of these is uncertain). The A_{2g} and A_{1u} modes are silent.

We have also applied the correlation method directly to the superlattice. The site group of the Ti atoms at the Wigner-Seitz cell center is $D_3(2)$, and the site group of the Ti atoms at the corners is $C_2(6)$. (The number of equivalent atoms in a site group is shown in parentheses.) The site group of the Se atoms at the corners is $C_3(4)$, and the site group of the Se atoms inside the cell is $C_1(12)$. The type and number of atoms in each

TABLE IV. Correlation diagram for the superlattice of $TiSe_2$. The labels a, d, f, and g are due to Wycoff as used in Ref. 18. For the A mode of C_1 the numbers along the lines indicate the number of lines between A and a representation of D_{3d}.

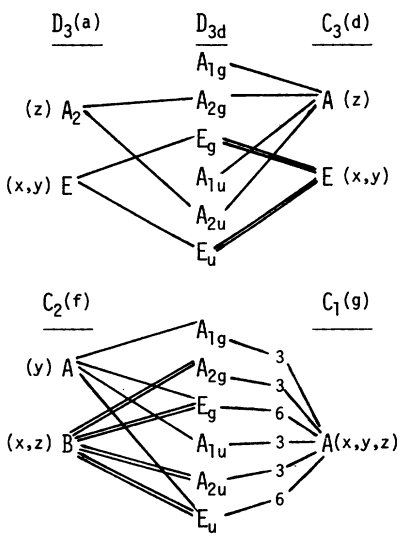

TABLE V. Decomposition of modes at the L and M points. The conventional notation of the representations has been given with the notation for the L point in parentheses.

C_{2h}	E (xyz)	C_2 $(\bar{x}y\bar{z})$	σ_h $(x\bar{y}z)$	i $(\bar{x}\bar{y}\bar{z})$
$T_{L,M}$	9	−1	3	−3

$T_{L,M} = 2A_g(L_1) + 2A_u(L_2) + B_g(L_3) + 4B_u(L_4)$

site is consistent with D_{3d}^4. The correlation diagram is given in Table IV and the number and symmetry of the modes agrees with Table III.

It is very informative to relate the modes at Γ in the superlattice to the modes in the $a_0 \times c_0$ lattice which have been folded into the new Brillouin zone center. The points A, L, and M of the original Brillouin zone are folded into Γ when a $2a_0 \times 2c_0$ superlattice forms. The group of the wave vectors at L and M is C_{2h} and the group of the wave vector at A is D_{3d} for a D_{3d} space group. The decomposition of the modes under C_{2h} is given in Table V. The principal axis C_2 of C_{2h} is the y axis (perpendicular to ΓM) in the Brillouin zone of Fig. 10. A more detailed assignment of the symmetries of translations of Ti and Se atoms is given in Table VI. The translations of the Se atoms are classified as odd under inversion through the Ti-site [e.g., x_u(Se)] if both Se atoms in the original unit cell move together and even [e.g., x_g(Se)] if they move in opposite directions.

There is an inversion of the parity of the modes at points A and L for the D_{3d}^4 space group of the superlattice relative to the D_{3d}^3 space group of the original lattice. The modes at A and L have a wave-vector component $\vec{q}_A$ along $\vec{z}$ so that displacements in the two adjacent layers are 180° out of phase. For such wave-vectors, inversion in D_{3d}^4 takes a Ti-displacement into itself while inversion in D_{3d}^3 (inversion center at a Ti atom) takes a Ti-displacement into the negative of itself. The same is true for x_u(Se) and z_u(Se). Conversely, the displacements x_g(Se), y_g(Se), and z_g(Se) become odd under the inversion operation in D_{3d}^4, whereas they were even under inversion in D_{3d}^3.

TABLE VI. Symmetry properties of translations of Ti and Se atoms for phonons at Γ, A, M, and L points of the original lattice.

Translations	$\Gamma, A(D_{3d})$	$M, L(C_{2h})$
x(Ti)	E_u	B_u
y(Ti)		A_u
x_u(Se)	E_u	B_u
y_u(Se)		A_u
z(Ti)	A_{2u}	B_u
z_u(Se)	A_{2u}	B_u
x_g(Se)	E_g	A_g
y_g(Se)		B_g
z_g(Se)	A_{1g}	A_g

TABLE VII. Correlation between irreducible representations at A, L, M, and Γ in space group D_{3d}^3 with those of Γ in D_{3d}^4.

A:	$A_{1g} \rightarrow A_{1u}$	$A_{2u} \rightarrow A_{2g}$
	$E_g \rightarrow E_u$	$E_u \rightarrow E_g$
L:	$A_g \rightarrow A_{1u} + E_u$	$A_u \rightarrow A_{1g} + E_g$
	$B_g \rightarrow A_{2u} + E_u$	$B_u \rightarrow A_{2g} + E_g$
M:	$A_g \rightarrow A_{1g} + E_g$	$A_u \rightarrow A_{1u} + E_u$
	$B_g \rightarrow A_{2g} + E_g$	$B_u \rightarrow A_{2u} + E_u$
Γ:	No change	

The correlation method is now applied to relate the modes of A, L, and M in the original lattice to those at Γ in the superlattice. After accounting for the parity change in the modes from the A and L points, we obtain the results shown in Table VII.

There should be a near degeneracy of the even parity modes from L and A with the odd parity from M and Γ, respectively and *vice versa*. There is probably not much dispersion of modes between M and L and between Γ and A, except possibly for the $A_u(L_2)$ mode which is coupled to the CDW, and the energies of the paired modes should be nearly degenerate. For example, the A_u mode from L gives $A_{1g} + E_g$ modes at Γ in the superlattice, but the A_u mode at M gives $A_{1u} + E_u$. These $A_{1u} + E_u$ modes from M are paired with these $A_{1g} + E_g$ modes from L. The A_{1u} mode is silent, and the pairing in the infrared and Raman spectra for these modes is only between E_u and $A_{1g} + E_g$.

V. DISCUSSION OF RESULTS

We now return to the Raman and infrared data, using wherever possible the predictions of the symmetry analysis of the previous section. The only strong new lines in the Raman spectrum of the CDW phase are an E_g mode at 74 cm^{-1} and an A_{1g} mode at 116 cm^{-1}; they also have a strong dependence on temperature. These are probably the CDW-coupled modes from the TA phonon at L. Some phonon dispersion curves have been measured from Γ to the L and A to M points by inelastic neutron scattering[19] and there are purely transverse phonons having energies of about 115 cm^{-1} at L and M. This frequency coincides well with the new 116 cm^{-1} A_{1g} mode in the Raman spectrum. It also coincides with the weak 118

cm^{-1} peak of the infrared data, which would be an E_u mode folded in from M rather than L. Although we do not yet have a detailed understanding of how the spectra evolve between 100 and 200 K, it appears that the 74 and 116 cm^{-1} modes behave differently, namely the former broadens rapidly with increasing temperature whereas the latter seems not to broaden but only to weaken.

The TA phonon polarized perpendicular to the basal plane and the LA phonon at L belong to B_u. These phonons would produce $2A_{2g}+2E_g$ modes at Γ in the superlattice. These could be assigned to the weak E_g peaks at 93 cm^{-1} and 148 cm^{-1}. Because the acoustic phonons belong to odd-parity representations and there is no inversion of parity from the M point phonons, we do not get any Raman-active modes from the acoustic phonons at M. We expect only one Raman-active E_g phonon from the basal-plane acoustic phonon E_u at the A point. This E_g mode corresponds to the E_{2g} interlayer mode in $2H$-MX_2 compounds. Dispersion curves for the acoustic phonons from Γ to A[13] show that the interlayer mode should have an energy of 30 cm^{-1}. We do not see this mode, presumably because its cross section is too small. The absence of this mode in the spectrum is unfortunate because its existence in Raman spectra would show that there is more than one layer in a unit cell of the superlattice.

The low temperature spectrum of $TiSe_2$ is not separated into distinct low-frequency and high-frequency regions from acoustic and optic phonons because the Se mass is larger than the Ti mass. In the Ta compounds, the metal mass is much larger than the S or Se mass, and there are well separated acoustic and optic regions. This allows the simplifying assumption that the charge density wave couples only to the motion of the Ta atoms.[20] In $TiSe_2$, the LA phonon at M actually has a larger energy (145 cm^{-1}) than the E_g optic phonon (134 cm^{-1}) at Γ.

The broad two-phonon peak near 300 cm^{-1} in Figs. 3 and 5 is probably due to two-phonon processes involving the highest acoustical branch at L and M, whose frequency is about 150 cm^{-1}. (See below). The broad two-phonon peak at 377 cm^{-1} is about twice the energy of the 190-cm^{-1} M point optic phonon. The 345-cm^{-1} peak might be due to a combination of these 190- and 150-cm^{-1} zone-boundary phonons, or it could be an overtone of the new 173-cm^{-1} A_{1g} mode. The 407-cm^{-1} peak could be an overtone of the 204-cm^{-1} A_{1g} mode. We believe that the E_g mode at 314 cm^{-1} is a combination of two infrared-active modes, namely the E_u modes at 137 and 175 cm^{-1}. This is allowed by symmetry since $E_u \times E_u = A_{1g}+A_{2g}+E_g$.

Finally, let us discuss the low-temperature far-infrared data shown in Fig. 8 and listed in Table II. We believe that the prominent features of these spectra above 90 cm^{-1} can be understood by folding zone-boundary modes of the normal crystal into Γ according to the assignments of Table VII. Remember that an infrared beam at normal incidence will couple only to E_u modes. Accurate knowledge of the lattice dispersion relations is essential and a certain amount of inelastic neutron diffraction data is available.[13,19] For example, Wakabayashi and Smith[19] have determined that at room temperature the acoustic branches intersect the zone boundary at M with the following frequencies (±10%): 150(B_u), 116(A_u), and 100 cm^{-1}(B_u). Higher frequency optical branches were found to intersect the zone-boundary face in the vicinity of 190 cm^{-1}. One of the observed optical branches originates in the nearly degenerate E_u and E_g modes at Γ around 135 to 140 cm^{-1}. The original E_u mode at Γ appears at 137 cm^{-1}. The strong 152-cm^{-1} peak in Fig. 8 probably arises by folding the uppermost acoustic branch (the 150-cm^{-1} B_u mode at M). The 175- and 198-cm^{-1} peaks most likely arise from optical branches, for example B_g at L and B_u at M (Refer to Table VII).

Some of the lower infrared frequencies can likewise be directly interpreted. The weak peak at 90 cm^{-1} could be related to the lowest acoustic branch at M (100 ± 10 cm^{-1},B_u). The reproducible feature at 118 cm^{-1} would come from the middle acoustic branch at M (116 cm^{-1},A_u). It is however more difficult to assign the bands superimposed upon the rising background due to free carrier absorption below 80 cm^{-1}. The 76-cm^{-1} infrared feature nearly coincides with the (softened) 74-cm^{-1} E_g mode of the Raman data which seems to be closely related to the charge density wave. On the other hand, the 74-cm^{-1} band has a somewhat different temperature dependence as mentioned earlier, and an E_g mode folded in from L should not be infrared active. Defects such as excess Ti might allow relaxation of the even-odd selection rules governing these processes, but this is unlikely since the relative strength of the 76-cm^{-1} infrared band does not change in nonstoichiometric crystals. Notice that there are three additional weak low-frequency lines in the ϵ_2 curve of Fig. 8. These are listed as 42, 52, and 64 cm^{-1} in Table II and corresponding features are not found in the Raman data. Of course it is conceivable that these as well as the 76-cm^{-1} peak are due to higher-order processes involving electron-hole excitation across narrow gaps below T_c as well as a very low frequency lattice mode. This is however highly speculative.

In the same spirit, one might also conjecture

that additional renormalization of lattice frequencies occurs at very low temperature. This might be related to another weaker unresolved phase transition or because of electron-hole spanning vectors which are not strictly from Γ to L. For example, vectors parallel to the ΓM direction might cause different renormalized frequencies in a strongly coupled electron-phonon system. The key to this interesting puzzle may be precise inelastic neutron data as a function of temperature, especially for the branch or branches of the lattice spectrum which appear to soften.

ACKNOWLEDGMENTS

We thank H. Smith and N. Wakabayashi for helpful discussions and D. Bruns for assistance in taking some of the Raman data.

---

‡Supported in part by the NSF under Grant DMR-76-01058.

*Present address: Mound Laboratory, Miamisburg, Ohio 45342.

[1]A. Zunger and A. J. Freeman (unpublished).

[2]J. A. Wilson and A. D. Yoffe, Adv. Phys. 18, 193 (1969).

[3]F. J. DiSalvo, D. E. Moncton, and J. V. Waszczak, Phys. Rev. B 14, 4321 (1976).

[4]R. Z. Bachrach, M. Skibowski, and F. C. Brown, Phys. Rev. Lett. 37, 40 (1976).

[5]M. M. Traum, G. Margaritondo, N. V. Smith, J. E. Rowe, and F. J. Di Salvo (unpublished); W. Fabian and C. H. Chen (private communication).

[6]J. A. Wilson and S. Mahajan, Comments Phys. 2, 23 (1977).

[7]K. C. Woo, F. C. Brown, W. L. McMillan, R. J. Miller, M. J. Schaffman, and M. P. Sears, Phys. Rev. B 14, 3242 (1976).

[8]W. Y. Liang, G. Lucovsky, R. M. White, W. Stutins, and K. R. Pisharody, Philos. Mag. 33, 493 (1976); Solid State Commun. 19, 303 (1976).

[9]P. M. Williams, in *Crystallography and Crystal Chemistry of Materials with Layered Structures*, edited by F. Levy (D. Reidel, Dordrecht, Holland, 1976), p. 51.

[10]A. H. Thompson, Phys. Rev. Lett. 35, 1786 (1975).

[11]C. A. Kukkonen and P. F. Maldague, Phys. Rev. Lett. 37, 782 (1976).

[12]G. Lucovsky, R. M. White, J. A. Benda, and J. F. Revelli, Phys. Rev. B 7, 3859 (1973).

[13]W. G. Stirling, B. Dorner, J. D. Cheeke, and J. Revelli, Solid State Commun. 18, 931 (1976).

[14]H. Schäfer, *Chemical Transport Reactions* (Academic, New York, 1965).

[15]R. C. Brandt, Applied Optics 8, 311 (1969).

[16]D. L. Grennaway and R. Nitsche, J. Phys. Chem. Solids 26, 1445 (1965).

[17]J. E. Smith, Jr., M. I. Nathan, M. W. Schafer, and J. R. Torrance, *Proceedings of the Eleventh International Conference on the Physics of Semiconductors* (Polish Scientific, Warsaw, 1972), p. 1306.

[18]*International Tables for X-ray Crystallograghy*, edited by N. F. M. Henry and K. Lonsdale (Kynoch Press, Birmingham, 1965), Vol. 1.

[19]N. Wakabayashi and H. Smith (private communication).

[20]J. A. Holy, M. V. Klein, W. L. McMillan, and S. F. Meyer, Phys. Rev. Lett. 37, 1145 (1976).